Dalton Transactions

ROYAL SOCIETY OF CHEMISTRY

PAPER

View Article Online
View Journal | View Issue

Cite this: *Dalton Trans.*, 2025, **54**, 11857

Bifunctional CoNi/MXene@Wood with vertical aperture structure for electromagnetic wave absorption and infrared stealth

Yuanyuan Li, [a] Mingqiang Ning, *[a] Zhe Zou,[a] Ming Gao[b] and Qikui Man[a]

Received 6th May 2025,
Accepted 3rd July 2025

DOI: 10.1039/d5dt01054c

rsc.li/dalton

Multifunctional integrated electromagnetic wave absorption (EMA) materials have been widely functional within the gigahertz range. Adjusting the electromagnetic parameters by decorating with magnetic/dielectric components to optimize the electromagnetic attenuation is an effective strategy for obtaining lightweight and efficient electromagnetic wave-absorbing materials. In this work, natural wood was pretreated by high-temperature carbonisation and polydopamine (PDA) modification, and CoNi and $Ti_3C_2T_x$-MXene were sequentially introduced into the pretreated carbonised wood with distinctive rectangular honeycomb cells by hydrothermal reaction and vacuum impregnation methods. Through structural design and material composition regulation, synergistic dielectric and magnetic loss effects were achieved. The optimized impedance endows CoNi/MXene@Wood-1.5 with a minimum reflective loss (RL_{min}) of −56.8 dB and an effective absorbing bandwidth (EAB) covering the entire X-band. Additionally, CoNi/MXene@Wood can realize the thermal infrared stealth of protected targets in different environments with low and stable thermal conductivity (0.219–0.267 W m^{-1} K^{-1}) over a temperature range of 298–673 K. The structural design and dielectric constant adjustment provide strategies for obtaining high EMA performance materials and infrared stealth applications.

Introduction

Everyday communication technologies such as mobile phones, computers, and other constantly changing digital devices generate electromagnetic wave (EMW) radiation, which can pose health risks[1–3] and has emerged as a new challenge for information security and public health. In addition, increasingly fierce military competition has promoted the development of various high-tech military equipment, especially the development of stealth fighters and unmanned aircraft,[4–6] which has resulted in considerable generation of electromagnetic radiation. Therefore, the development of electromagnetic wave absorption (EMA) materials is critical and is becoming an essential part of civil and military fields.

Satisfying EMA performance through magnetic loss capacity can be obtained by traditional magnetic materials such as ferrite.[7] However, ferrites are always limited by high filling ratios and weight. Newly developed carbon materials including carbon nanotubes (CNTs)[8] and graphene[9,10] are considered promising in EMA due to their high specific surface area and low density. As a result, carbon-based foams, carbon–carbon polymer composites, and carbon-ferrite composites are satisfactory candidates to achieve effective EMA properties.[11,12] However, the microstructure of most porous carbon EMA materials is irregular, and the random structure may result in excessive reflection at the interface, thereby reducing the EMA capacity. Therefore, in recent years, integrating structure and function has emerged as a key strategy for improving carbon-based EMA materials. Developing novel carbon-based EMA materials with well-organised microporous structures is of great significance.

At present, the general methods for constructing structure–function integrated carbon-based composite EMA materials are as follows: first, three-dimensional (3D) porous structures are obtained by self-assembly of one-dimensional (1D)/two-dimensional (2D) carbon materials. Subsequently, enhancement by decorating with magnetic particles achieves impedance matching of the material.[13–16] However, it is difficult to control the orientation of the structure during self-assembly, and the preparation process is complex. In addition, compared with single-hole structures assembled by one-dimensional/two-dimensional materials, the synergistic advantage of layered porous structures is the more optimal performance of their multi-dimensional structural units.[17] The layered structure causes EMWs to detour between the composite layers. It also amplifies microwave and visible light reflection while

[a]*Zhejiang Provincial Key Laboratory of Magnetic Materials and Applications, Ningbo Institute of Materials Technology and Engineering of the Chinese Academy of Sciences, Ningbo, Zhejiang 315201, China. E-mail: ningmingqiang@nimte.ac.cn*
[b]*Metals and Chemistry Research Institute, China Academy of Railway Sciences Corporation Limited, Beijing 100081, China*

offering conduction losses and thermal insulation. This increases the absorption of EMWs.[18–20] Thus, it is difficult to prepare a layered porous carbon material with excellent EMA properties.

In contrast to synthetic materials with irregular structures, some natural materials, such as wood, exhibit highly ordered microstructures. Taking advantage of this feature, natural wood has been directly designed as a functional material in recent years, such as catalytic materials,[21] supercapacitors,[22] and lithium-ion batteries.[23] In addition, research has been performed on EMA and electromagnetic shielding. For example, the ordered parallel channel structure of PBPC prepared by Xi *et al.* displays a reflection loss of −68.3 dB and a maximum effective absorption bandwidth (EAB) of 7.63 GHz.[24] Xiong and co-workers constructed FeCo/C@WC based on wood, which achieved −47.6 dB RL_{min} and a maximum EAB of 8.9 GHz.[17] Therefore, the highly ordered microstructure of wood can be wisely used to design a 3D interconnected structure to achieve excellent EMA performance.

Magnetic metals including iron, cobalt, nickel, and their alloys exhibit greater magnetic loss than ferrite. In recent years, there has been considerable utilization of CoNi alloy particles due to their high Curie temperature, high permeability, and excellent oxidation resistance.[25] Because of the strong correctivity and high saturation magnetization strength of CoNi alloy particles, they are more favorable for high EMA properties. For example, Zhao *et al.* successfully prepared CoNi@NCPs-rGO composites and obtained excellent EMA performance with an RL_{min} value of −58.2 dB at 2.5 mm thickness.[26] Guo *et al.* synthesized CoNi alloy/N-doped hollow carbon foam (CoNi/NCF) *via* a hydrothermal reaction, using melamine foam as the precursor. Introducing suitable CoNi alloys effectively regulated the EMA properties of NCF. The CoNi/NCF composite achieved an RL_{min} value of −47.35 dB and a maximum EAB of 5.6 GHz at a thickness of 2.4 mm, demonstrating excellent EMA performance.[27]

In another study, Qiu *et al.* prepared two-dimensional CoNi@MC composites using CoNi LDH@MPDA as the precursor. Because of its heterogeneous structure and dual-loss mechanism, the CoNi@MC material exhibited remarkable microwave absorption properties, achieving a maximum reflection loss of −70.86 dB and a broad EAB of 7.74 GHz.[28] The introduction of magnetic CoNi alloy particles into wood may be an excellent structural solution for EMA composites.

The dielectric loss provided by carbonized wood (C-Wood) alone, however, seems to be inadequate and cannot provide sufficient attenuation of EMW. In recent years, MXene has been a promising candidate for EMA materials applications because of its unique dielectric loss capability and low density.[29–31] The orderly layered MXene structure prepared by Cui *et al.* achieved an RL_{min} of −45.2 dB at 1.5 mm. Thanks to effective electron movement at the nanoscale, the boosted conduction and polarization losses greatly improved the electromagnetic wave absorption ability.[32] Fan and co-workers investigated the effect of different layer spacings between MXene sheets on the absorption performance, and because of its unique 2D structure as well as the enhancement of the space charge polarization effect, MXene RL_{min} reached −36.3 dB.[33]

Cheng *et al.* prepared multifunctional Ni/MXene MF *via* electrostatic self-assembly and a dip-coating process. The thermal insulation, infrared stealth, and flame retardancy of the material are excellent. It achieves an RL_{min} of −62.7 dB and a corresponding EAB of up to 6.24 GHz at a thickness of merely 2 mm.[13] Chen *et al.* developed a liquid metal-MXene-based hierarchical aerogel with radar-IR compatible camouflage. With a material density of 4.4 mg cm^{-3}, it delivers a maximum reflection loss of −73.2 dB and an adjustable absorption bandwidth of up to 7 GHz.[34] Gao *et al.* created lightweight 3D hierarchical ordered porous structures (3D OPMR) based on MXene and ReS_2 using a directional freeze-drying technique. The porous backbone, nanostructure, and multilayer structure optimized the heterogeneous interface, while the unique hierarchical pore structure imparted excellent infrared stealth performance.[35] Thus, MXene is a satisfactory EMA material, and its attenuation of EMW mainly depends on dielectric loss. Therefore, introducing MXene into wood will favorably increase the dielectric loss capacity and EMA efficiency.

Herein, CoNi/MXene@Wood was fabricated using carbonised wood as the substrate, with CoNi/MXene introduced *via* a hydrothermal reaction and a vacuum impregnation process. CoNi/MXene@Wood integrates the advantages of natural wood, CoNi alloy particles, and MXene with richer multi-dimensional hierarchical pore structure, increased contact continuity, and greater uniform distribution of magnetic functional particles. When the incident EMWs pass through the prepared CoNi/MXene@Wood, the multiple reflections and scattering within the wood pore channel lead to a rapid decrease in reflected and transmitted waves due to the magnetic loss provided by the CoNi alloy particles and the dielectric loss provided by MXene. By adjusting the immersed amount of MXene and CoNi, the dielectric and magnetic properties of the composite can be well-tuned to provide the optimum EMA performance.

A −56.8 dB RL_{min} value was obtained with the prepared CoNi/MXene@Wood-1.5, and it can cover the entire X-band. Moreover, CoNi/MXene@Wood displayed low and stable thermal conductivity (0.219–0.267 W m^{-1} K^{-1}) over a temperature range of 298–673 K, and therefore, it can be used as an infrared stealth material for practical applications. In view of its light weight, relatively low cost, and the easy development of wood, wood-based functionalized materials demonstrate satisfactory prospects for applications in the field of wave absorption and stealth.

Experimental section

Materials and chemicals

Pine wood was obtained from Shengzhilin Company. Dopamine hydrochloride (98%, Macklin) and Tris-HCl (99.9%, Macklin) were used for the synthesis of the PDA coating layer.

Cobalt(II) acetate tetrahydrate ($(CH_3COO)_2Co{\cdot}4H_2O$, 99.9%, Aladdin), nickel(II) acetate tetrahydrate ($(CH_3COO)_2Ni{\cdot}4H_2O$, 99.9%, Aladdin), ethylene glycol (99%, Aladdin), and sodium hydroxide (NaOH, 98%, Aladdin) were used for the preparation of CoNi. Ti_3AlC_2 (98%, 400 mesh, Aladdin), LiF (99.99%, Aladdin), and HCl (AR, Sinopharm) were used for the preparation of $Ti_3C_2T_x$ MXene.

Synthesis of CoNi@Wood

The pine wood was cut into 5 mm thick slices along the radial direction, and the obtained wood slices were pre-oxidized at 523 K for 2 h. After pre-oxidation, the wood slices were carbonized in Ar at 948 K for 4 h with a heating rate of 5 K min^{-1}. The C-Wood slices were carefully polished with 400 and 1000 grit sandpaper to obtain a thickness of 2 mm. Residual carbon was removed by ultrasonic washing. Then, the C-Wood was immersed in Tris-HCl buffer solution (10 mM, pH ≈ 8.5) containing dopamine hydrochloride (2 mg ml^{-1}) for 8 h. During this process, dopamine undergoes spontaneous oxidization and self-polymerization to form a PDA layer that was densely coated onto the C-Wood surface.

Finally, 3 mmol $(CH_3COO)_2Co{\cdot}4H_2O$ and 3 mmol $(CH_3COO)_2Ni{\cdot}4H_2O$ were dissolved in 40 ml ethylene glycol under stirring for 30 min. Then, 18 mmol NaOH was added, with continued stirring until it was completely dissolved. The PDA-coated C-Wood was vacuum-impregnated in the above solution for 2 h, and then transferred to a 50 mL Teflon-lined stainless steel autoclave and reacted at 473 K for 12 h. After the reaction was completed, the sample was washed with water and ethanol and dried to obtain CoNi@Wood.

Synthesis of $Ti_3C_2T_x$ MXene

$Ti_3C_2T_x$ MXene was synthesized *via* etching the Ti_3AlC_2 phase with LiF/HCl according to our previous work.[36] In a typical synthesis process, 2 g LiF powder was added to 40 mL HCl solution, with stirring for 40 min at room temperature. Then, 2 g Ti_3AlC_2 powder was slowly added to the solution. After that, the mixture was maintained in a water bath at 35 °C under continuous stirring for 24 h. Then, the obtained solution was repeatedly washed with deionized water by centrifugation (4000 rpm, 2 min) until the pH >6. Multilayer $Ti_3C_2T_x$ MXene was then obtained. After that, with the assistance of ultrasound treatment for 3 h, the multilayered $Ti_3C_2T_x$ was exfoliated into few-layered or monolayered $Ti_3C_2T_x$ nanosheets. Finally, the unexfoliated $Ti_3C_2T_x$ was removed by centrifuging at 8000 rpm for 20 min. The dark-green supernatant containing $Ti_3C_2T_x$ MXene nanosheets was collected, and $Ti_3C_2T_x$ MXene powder was obtained after a freeze-drying treatment.

Synthesis of CoNi/MXene@Wood

CoNi@Wood was immersed in $Ti_3C_2T_x$ MXene solution (0.5, 1.0, 1.5, and 2.0 mg ml^{-1}) and then transferred into a vacuum oven under 100 Pa to remove air. The above solid–liquid mixtures were then frozen in liquid nitrogen, followed by freeze-drying for 48 h. The samples with different $Ti_3C_2T_x$ MXene concentrations of 0.5, 1.0, 1.5, and 2.0 mg ml^{-1} are denoted as CoNi/MXene@Wood-0.5, CoNi/MXene@Wood-1.0, CoNi/MXene@Wood-1.5, and CoNi/MXene@Wood-2.0, respectively.

Characterization

The morphology and microstructure of the samples were investigated with scanning electron microscopy (SEM, Zeiss G300) and transmission electron microscopy (TEM, FEI Talos F200x). The crystalline properties of all absorbers were obtained using X-ray diffraction (XRD, Cu K_α radiation). The complex dielectric constant and permeability of all absorbers were measured over 8–12 GHz by a vector network analyzer (VNA, Agilent N5234A) using the waveguide test system. To meet the waveguide holder requirements, all samples were cut into rectangular blocks with dimensions of approximately 22.8 × 10.6 × 2.0 mm^3. The thermal conductivity of the samples at different temperatures was characterized using a laser thermal conductivity analyzer (NETZSCH-LFA). Thermal infrared images were obtained using an infrared camera (FLIR-A325SC).

Results and discussion

Fig. 1 shows a schematic of the preparation process for CoNi/MXene@Wood composites. After carbonization, natural wood retains a large number of straight, regular porous channels along the tree growth direction that not only effectively prevent heat transfer but also provide ideal interfaces for multiple reflections of EMWs. In addition, the porous channels of C-Wood allow decoration with CoNi alloy particles and $Ti_3C_2T_x$ MXene. To provide active sites for the growth of CoNi alloy particles, a layer of PDA was coated onto the surface of C-Wood. Subsequently, CoNi alloy particles were grown *in situ* in the pore channels of C-Wood by hydrothermal reaction to obtain CoNi/Wood. Finally, $Ti_3C_2T_x$ MXene was injected into the CoNi/Wood pore channels by vacuum impregnation, and CoNi/MXene@Wood was successfully prepared.

The micromorphological evolution of the materials was studied by SEM. Fig. 2(a and b) shows the rectangular honeycomb structure of C-Wood along the parallel growth direction with an average cell size of 30 × 15 μm and a long channel structure along the vertical growth direction. To further improve the EMA performance, CoNi and $Ti_3C_2T_x$ MXene were introduced into a rectangular cellular unit inside C-Wood. As shown in Fig. 2(c), the size of the prepared CoNi alloy particles is approximately 1 μm. Fig. 2(d) shows a single layer of $Ti_3C_2T_x$ MXene with a lateral size of approximately 500 nm, indicating that the Al layer was successfully etched by the Ti_3AlC_2 MAX phase. Moreover, it can be observed from the atomic force microscopy (AFM) image in Fig. 2(e) that the $Ti_3C_2T_x$ MXene nanosheet is very thin and flat, with a thickness of approximately 3 nm.

CoNi and $Ti_3C_2T_x$ MXene are sufficiently small in size to facilitate their introduction into C-Wood. The CoNi/Wood displayed in Fig. 3(a) shows the uniform distribution of the CoNi alloy particles on the C-Wood skeleton. Based on this, the $Ti_3C_2T_x$ MXene was decorated, and its presence becomes more

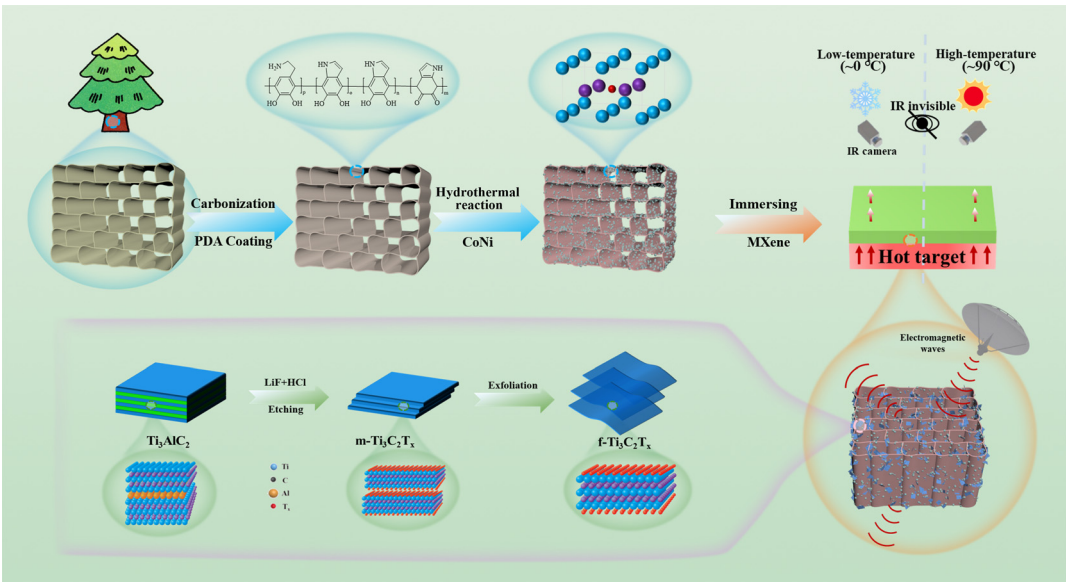

Fig. 1 Schematic of the preparation of CoNi/MXene@Wood.

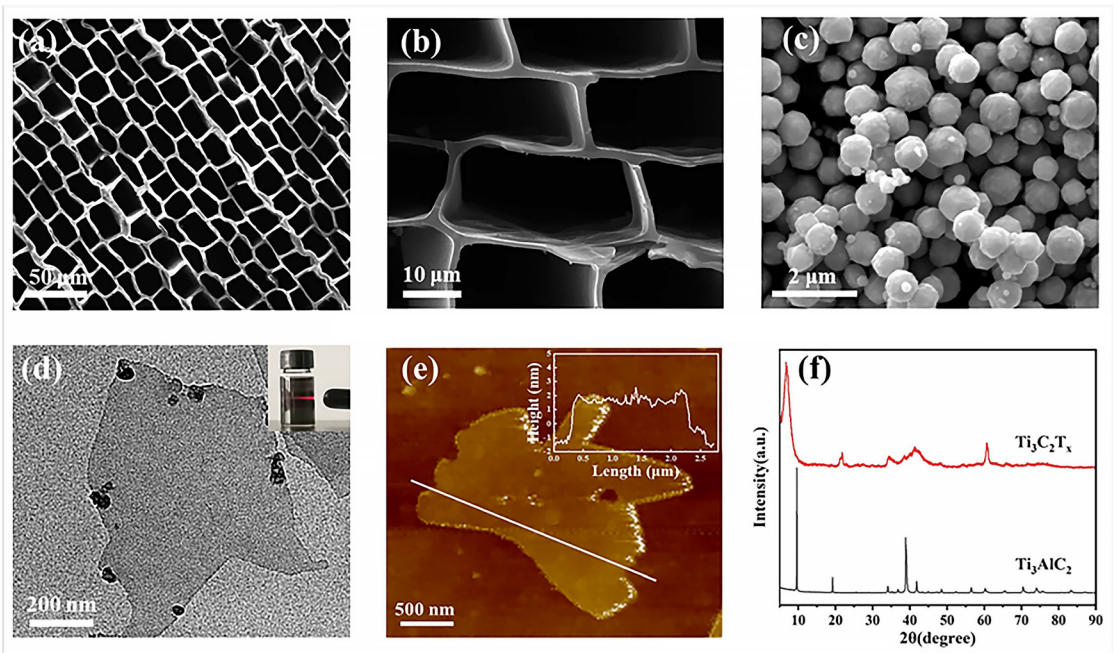

Fig. 2 SEM images of (a) cross-sectional wood, (b) high-magnification cross-sectional wood, and (c) CoNi. (d) TEM image of $Ti_3C_2T_x$ MXene. (e) AFM image of $Ti_3C_2T_x$ MXene. (f) XRD patterns of Ti_3AlC_2 and $Ti_3C_2T_x$ MXene.

pronounced as the concentration increases (Fig. 3(b–e)). In addition, energy dispersive X-ray spectroscopy (EDS) analysis of the CoNi/MXene@Wood-1.5 composites, as shown in Fig. 3 (g–j), reveals a uniform distribution of Ni, Co, and Ti, further demonstrating the successful distribution of CoNi/MXene adhered onto C-Wood. The introduction of CoNi alloy particles and MXene significantly enriches the heterogeneous interfaces of the composites. When EMW interacts with the composites, charge accumulation at the interfaces forms 'macroscopic' dipole moments and local electric fields. These formations enhance interfacial polarization, thereby boosting dielectric loss.

XRD was employed to analyze the crystal structures of CoNi/MXene@Wood. In the XRD spectra (Fig. 3(f)), all absorbers display two wide peaks at approximately 23° and 44°, which correspond to the (002) and (100) diffraction of graphite,[24] respectively. Two diffraction peaks of the (111) and (200) lattice plane of the face-centered cubic phase of CoNi alloy (JCPDS

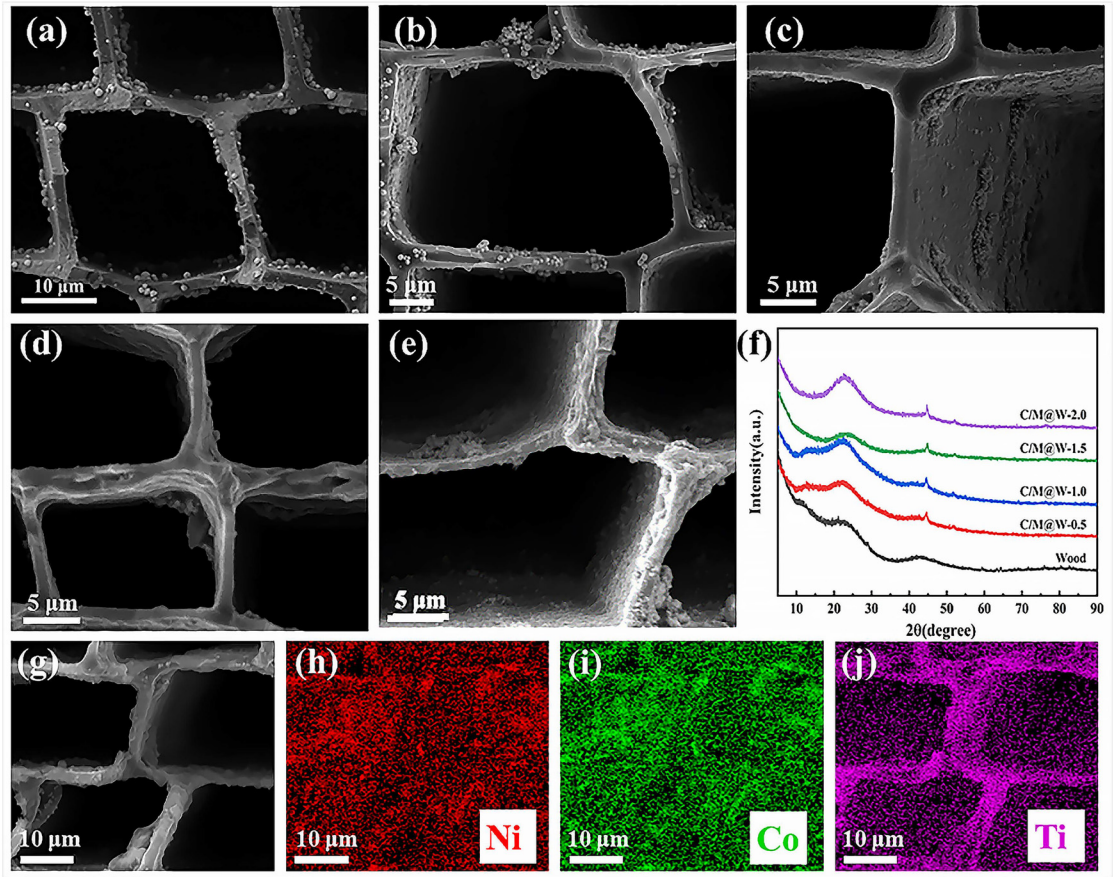

Fig. 3 SEM image of (a) CoNi@Wood, (b) CoNi/MXene@Wood-0.5, (c) CoNi/MXene@Wood-1.0, (d) CoNi/MXene@Wood-1.5, and (e) CoNi/MXene@Wood-2.0. (f) XRD patterns of wood and CoNi/MXene@Wood. (g) SEM images of CoNi/MXene@Wood-1.5 and its homologous EDS elemental mapping of (h) Ni, (i) Co, and (j) Ti.

no. 89-4307) were also detected in CoNi/MXene@Wood-0.5, CoNi/MXene@Wood-1.0, CoNi/MXene@Wood-1.5, and CoNi/MXene@Wood-2.0 at approximately 44.5° and 51.6°, respectively.[37] It was demonstrated that CoNi was successfully grown in rectangular cellular units of C-Wood. However, the peaks corresponding to $Ti_3C_2T_x$ MXene (Fig. 2(f)) were not detected, which may be due to the low content of $Ti_3C_2T_x$ MXene. This phenomenon has been also reported in a previous work.[36]

According to the transmission line theory,[38–40] the EMA efficiency of CoNi/MXene@Wood was evaluated by RL value as follows:

$$Z_{in} = Z_0\sqrt{\frac{\mu_r}{\varepsilon_r}}\tanh\left(j\frac{2\pi f t_m}{c}\sqrt{\mu_r\varepsilon_r}\right) \quad (1)$$

$$RL = 20\log\left|\frac{Z_{in}-Z_0}{Z_{in}+Z_0}\right| \quad (2)$$

where Z_{in} denotes the input impedance of the absorber, Z_0 denotes the free space impedance, μ_r and ε_r denote the relative complex permeability and dielectric constant, respectively; f denotes the EMW frequency, t_m denotes the thickness of the absorber, and c denotes the speed of light. Fig. 4 shows the RL-f curve of wood, CoNi/MXene@Wood-0.5, CoNi/MXene@Wood-1.0, CoNi/MXene@Wood-1.5, and CoNi/MXene@Wood-2.0 under 1.0, 1.5, 2.0, 2.5, 3.0, 3.5, 4.5, and 5.0 mm over 8–12 GHz. The RL_{min} of pure wood is more than −10 dB at a greater thickness. With the introduction of CoNi/MXene, the EMA performance of all absorbers has been improved, with effective bandwidth covering the entire X-band. However, when the content of $Ti_3C_2T_x$ MXene is excessively low, the EMA capability of CoNi/MXene@Wood-0.5 and CoNi/MXene@Wood-1.0 is relatively weak (−16.7 dB and −15.8 dB), and the corresponding thickness is 4.0 mm when the effective bandwidth can cover the entire X-band. With an increase in $Ti_3C_2T_x$ MXene content, CoNi/MXene@Wood-1.5 reveals more attractive EMA properties.

The RL_{min} value reaches −56.8 dB at 9.9 GHz with a thickness of 3.0 mm and can cover the entire X-band. CoNi/MXene@Wood-2.0 with higher $Ti_3C_2T_x$ MXene content displays an RL_{min} of −60.4 dB, and the corresponding thickness is 3.5 mm. There is little difference in EMA strength, and both of them can cover the X-band. The EMA performance of CoNi/MXene@Wood-1.5 is optimum. Overall, the introduction of CoNi/MXene and regulation of the MXene content resulted in significant improvements in EMA strength, effective band-

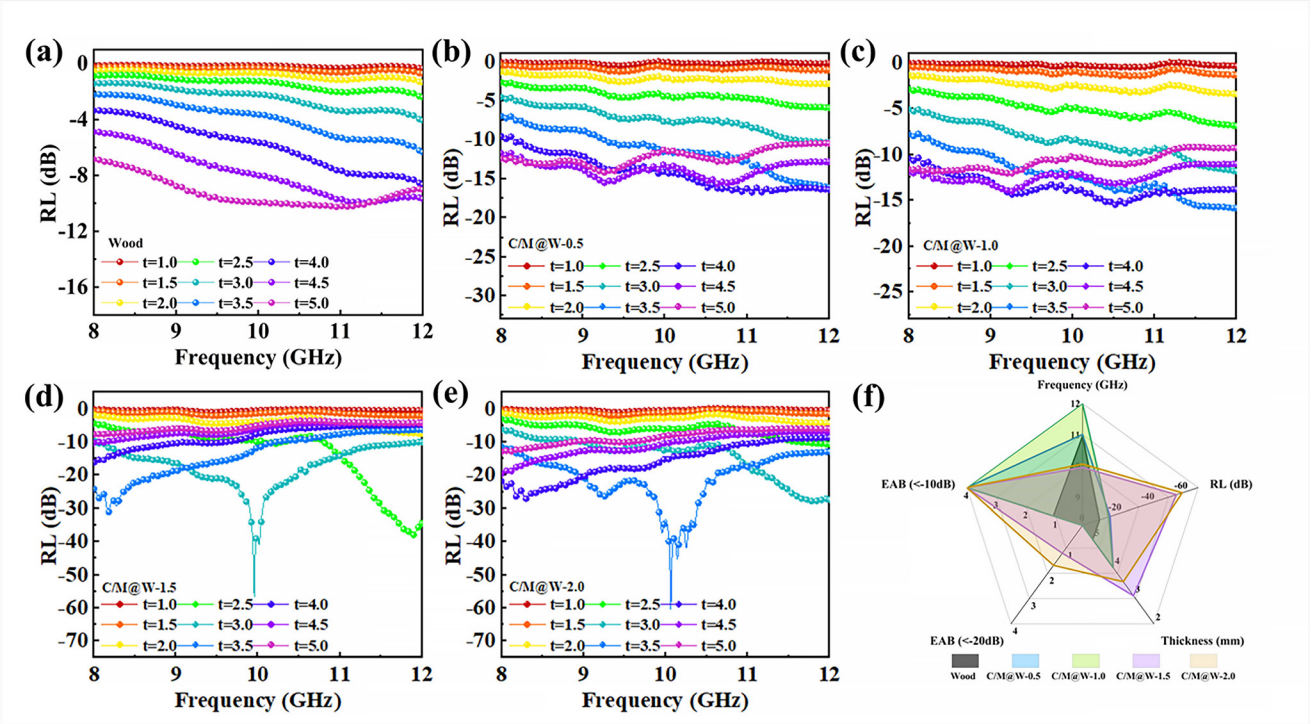

Fig. 4 RL values of (a) wood, (b) CoNi/MXene@Wood-0.5, (c) CoNi/MXene@Wood-1.0, (d) CoNi/MXene@Wood-1.5, (e) CoNi/MXene@Wood-2.0, and (f) a data radar chart of CoNi/MXene@Wood.

width, and corresponding thickness, thereby effectively optimizing the EMA performance of the composite (Fig. 4(f)).

The EMA performance of materials is largely influenced by electromagnetic parameters, which were examined to explore the attenuation mechanisms of materials. On this basis, through the waveguide method to determine the Wood, CoNi/MXene@Wood-0.5, CoNi/MXene@Wood-1.0, CoNi/MXene@Wood-1.5, and CoNi/MXene@Wood-2.0 complex dielectric constant ($\varepsilon_r = \varepsilon' - j\varepsilon''$) and complex permeability ($\mu_r = \mu' - j\mu''$), including ε' and μ' on behalf of the electric and magnetic energy storage, ε'' and μ'' represent the corresponding loss.

The relation between dielectric constant and complex permeability and frequency is shown in Fig. 5. It can be seen that with the increase in the $Ti_3C_2T_x$ MXene content, ε' demonstrates an overall upward trend, indicating the composites' enhanced ability to store electrical energy.[41] CoNi/MXene@Wood-1.5 and CoNi/MXene@Wood-2.0 show abnormal increases, which may result from excessive MXene accumulation.[35] The trend of ε'' is opposite to that of ε', as ε'' primarily depends on polarization loss (ε_p'') and conduction loss (ε_c''). Herein, $\varepsilon_c'' = \sigma/(2\pi f \varepsilon_0)$, where ε_0 denotes vacuum permittivity, σ denotes electrical conductivity, and f represents frequency.[42] With the increase in MXene content, ε'' slightly decreases due to the disruption of the original conductive network as a result of the high conductivity of MXene.[43] The ε'' of CoNi/MXene@Wood is much greater than that of wood, indicating that the introduction of CoNi alloy particles and $Ti_3C_2T_x$ MXene enhances the dielectric loss.

The content of $Ti_3C_2T_x$ MXene has little effect on the μ_r, and there is little change in μ' and μ'', but the μ' of CoNi/MXene@Wood is significantly higher than that of wood, which is mainly due to the contribution of the CoNi alloy. The μ' fluctuations may result from ferromagnetic resonance or local magnetic field distortions near defects. The μ'' and tan $\delta\mu$ show similar trends, with more pronounced curve fluctuations. These peaks stem from energy loss during the material's resonance process.

The prerequisite for electromagnetic wave-absorbing materials to fully realize their excellent wave-absorbing performance is to achieve excellent impedance matching. This entails the transmission of most of the incident EMWs through the surface of the material into the interior, where further EMW energy loss occurs. Impedance matching is a prerequisite for designing wave-absorbing materials, as shown by the equation $Z = |Z_{in}/Z_0|$, where the impedance of the material surface should be as close as possible to the characteristic impedance of free space.[44–46] As analyzed in Fig. 5(g), the impedance matching of the modified composites CoNi/MXene@Wood-x (where x = 0.5, 1.0, 1.5, and 2.0) is significantly better than that of pure wood. This improvement is attributed to the introduction of CoNi/MXene, which modulates the electromagnetic properties of the composites.

The enhanced performance is likely due to a synergistic interaction between dielectric and magnetic losses, optimizing the impedance matching. The introduction of CoNi/MXene produces abundant heterogeneous interfaces, which enhance

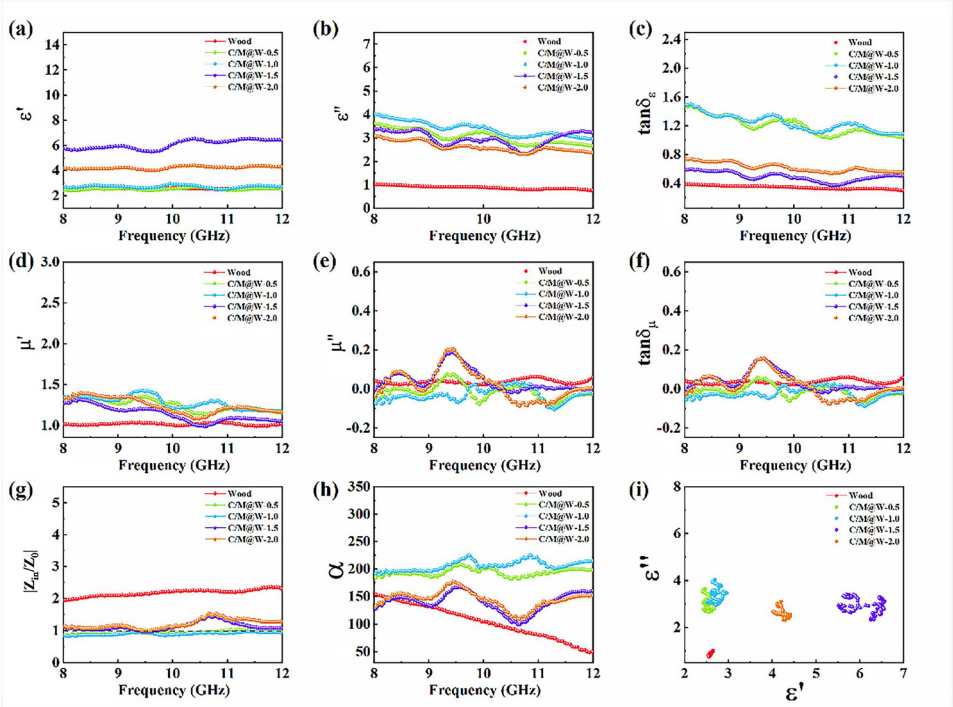

Fig. 5 (a) Real parts, (b) imaginary parts of permittivity, and (c) dielectric loss tangent tan δ_ε. (d) Real parts, (e) imaginary parts of permeability, (f) magnetic loss tangent tan δ_μ, (g) impedance matching, (h) attenuation coefficient α, and (i) Cole–Cole plots of Wood, CoNi/MXene@Wood-0.5, CoNi/MXene@Wood-1.0, CoNi/MXene@Wood-1.5, and CoNi/MXene@Wood-2.0.

the interfacial polarisation effect due to the difference in electrical conductivity between the different constituents, and improve the dielectric loss. Specifically, the introduction of the two-dimensional multilayer structure $Ti_3C_2T_x$ MXene not only improves the electrical conductivity of the material but also enhances the multiple reflections of the incident EMWs. This prolongs the transmission path of the EMWs and strengthens the EMW loss. From the analysis of Fig. 5(e–g), it is clear that the addition of the CoNi magnetic particles mainly serves to optimize impedance matching, allowing dielectric loss and magnetic loss to produce a synergistic effect. This synergy facilitates the entry of additional EMWs into the material's interior and enhances the attenuation of EMW energy.

EMA materials must also possess excellent EMW attenuation properties, in addition to satisfactory impedance matching. The conversion of EMW energy is determined by the absorption attenuation characteristics, which can be characterized by the attenuation coefficient (α). The value of α can be calculated according to the following equation:[44,47,48]

$$\alpha = \frac{\sqrt{2}\pi f}{c} \times \sqrt{(\mu''_r\varepsilon''_r - \mu'_r\varepsilon'_r) + \sqrt{(\mu''_r\varepsilon''_r - \mu'_r\varepsilon'_r)^2 + (\mu'_r\varepsilon''_r - \mu''_r\varepsilon'_r)^2}}. \quad (3)$$

The fluctuations in the α function curves are the result of the combined effects of conductivity loss, polarization loss, and eddy current loss within the samples.[49] As shown in Fig. 5(h), the order of magnitude of α values are as follows: Wood < CoNi/MXene@Wood-2.0 (approximate to CoNi/MXene@Wood-1.5) < CoNi/MXene@Wood-1.0 (approximate to CoNi/MXene@Wood-0.5) in the studied frequency range. This trend is generally consistent with tan δ_ε.

This result further confirms that the attenuation of electromagnetic energy in composites is primarily determined by dielectric loss. The attenuation loss capability of the modified composite CoNi/MXene@Wood-x (x = 0.5, 1.0, 1.5, and 2.0) is significantly higher than that of pure wood, with CoNi/MXene@Wood-1.0 exhibiting the highest attenuation loss capability. However, the most optimal wave absorption performance was not achieved by CoNi/MXene@Wood-1.0, as shown in Fig. 4. This indicates that the wave absorption performance depends not only on the overall loss capability, but also on impedance matching, which is a prerequisite.

As the MXene content increases, Fig. 5(g) shows that the curves for CoNi/MXene@Wood-1.5 and CoNi/MXene@Wood-2.0 peak in the high-frequency range. This is due to the impedance mismatch caused by the Z value being much larger than 1.[50] Combined with the previous electromagnetic parameter analysis, this phenomenon can be attributed to the skin effect. The combined effect results in CoNi/MXene/Wood-1.5 composites exhibiting the most optimal EMA properties due to their excellent impedance characteristic matching and satisfactory attenuation properties.

To further analyze the type of polarisation loss in composites, the Debye relaxation theory was employed to describe

the complex dielectric constant and the dielectric response characteristics at different frequencies. This theory also assists in the analysis of the dielectric relaxation behavior of the medium, and the Debye relaxation theory describes the relation between ε' and ε'' as follows:[51–53]

$$\left(\varepsilon' - \frac{\varepsilon_s - \varepsilon_\infty}{2}\right)^2 + (\varepsilon'')^2 = \left(\frac{\varepsilon_s - \varepsilon_\infty}{2}\right)^2 \quad (4)$$

where ε_s denotes the static dielectric constant, and ε_∞ denotes the dielectric constant in the high-frequency limit. A complete polarisation process $\varepsilon' - \varepsilon''$ diagram will feature one or more Cole–Cole semicircles, which exhibit different characteristics in the low- and high-frequency bands. These semicircles can be used to determine the presence of relaxation polarization in a dielectric.[54–56] Polarisation relaxation occurs when the charge in a dielectric is restricted by defects or functional groups and cannot move as freely as electrons in an external electric field. This relaxation occurs when the polarization process of a material fails to advance with the frequency changes of the electromagnetic field.

Dielectric loss is the characteristic electronic interaction between the electric field and the wave-absorbing material, and it consumes the energy of the EMW.[57] It is primarily caused by conductive loss and polarization loss, with dipole polarization and interface polarization mainly occurring in the microwave region (2–18 GHz). Fig. 5(i) shows that CoNi/MXene@Wood-1.5 exhibits three distinct semicircles, indicating the presence of multiple polarization relaxation processes in the material. These processes may be generated by the dipole polarisation of the bound charges at the defects in the carbon matrix, the dipole polarisation of the residual groups, or the interfacial polarisation between the composite CoNi/MXene and the carbon matrix. These results suggest that the introduction of $Ti_3C_2T_x$ MXene enhances the dielectric loss.

By synthesizing the EMA mechanism of the composites above, the improvement in the wave-absorbing performance of CoNi/MXene@Wood composites can be analyzed according to the following two aspects. (1) The addition of two-dimensional carbon material $Ti_3C_2T_x$ MXene and CoNi alloy particles, which results in the synergistic effect of the dielectric and magnetic properties. This significantly optimizes the impe-

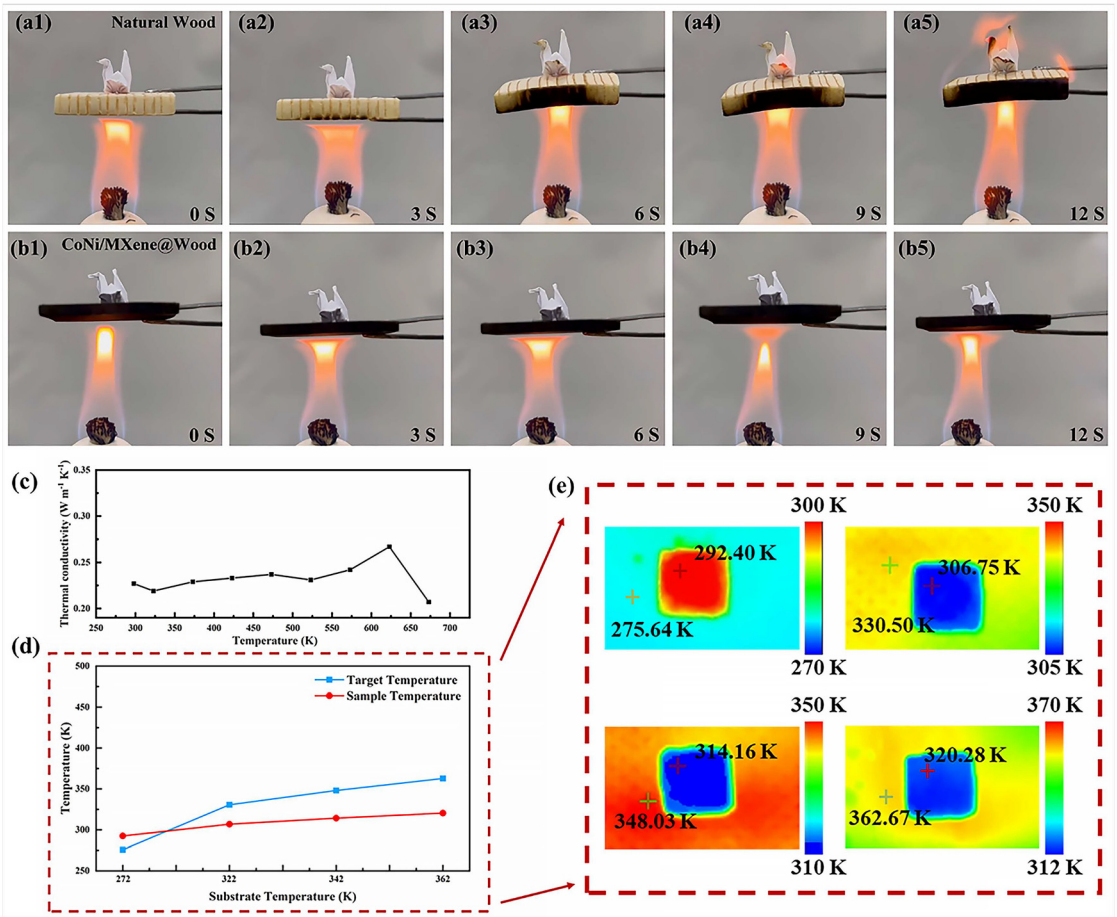

Fig. 6 Photographs of a paper crane placed on (a1–a5) natural wood and (b1–b5) CoNi/MXene@Wood composites heated by flame during different time periods. (c) Thermal conductivity of CoNi/MXene@Wood at different temperatures. (d and e) Thermal infrared image of CoNi/MXene@Wood in low-temperature and high-temperature environments.

dance matching of the composites, providing favorable conditions for the attenuation of incident EMWs. CoNi alloy particles can cause magnetic losses, such as eddy current loss and ferromagnetic resonance, which also occur and attenuate EMWs. Additionally, $Ti_3C_2T_x$ MXene enhances the conductive loss of the material because of its high conductivity. (2) The EMW energy loss of CoNi/MXene@Wood composites is dominated by dielectric loss, which primarily comes from the effect of conductive loss and polarisation loss. The natural wood was carbonized to create a unique pore structure, and was loaded with CoNi alloy particles and $Ti_3C_2T_x$ MXene after undergoing polydopamine (PDA) modification. This enables the incident EMW to enter the interior of the material for multiple reflections and scattering, which prolongs the EMW transmission path and enhances the EMA. Additionally, the incorporation of CoNi/MXene components greatly enriches the heterogeneous interfaces of the composites. The surface defects and functional groups (–O, –OH, and –F, *e.g.*) on MXene nanosheets serve as polarization centers. When electromagnetic waves act on composites, these defects and functional groups induce oscillations that initiate interfacial polarization, dipolar polarization, and defect-related polarization. These mechanisms jointly enhance the polarization loss properties of the composites.

In addition to EMWs interference, for variable-frequency electronic devices in different operating conditions, their surface temperatures often vary significantly from the surrounding environment, which will result in a remarkable radiation contrast in thermal images, thus reducing the thermal infrared stealth performance of some military and industrial targets. It is necessary to blend the protected targets into the background in thermal images to dodge infrared detection. The thermal insulation properties of carbonized wood are known to be satisfactory due to its porous structures.

The paper cranes were placed on natural wood and CoNi/MXene@Wood-1.5, both of which were heated with a flame, as shown in Fig. 6(a and b). It was found that at continuous heating for 6 s, the paper crane placed on natural wood began to turn black and burned completely at 12 s. In contrast, the paper crane placed on CoNi/MXene@Wood-1.5 exhibited no change during each period, suggesting that CoNi/MXene@Wood-1.5 possessed excellent thermal insulation. The synergy of structure and composition enables CoNi/MXene@Wood-1.5 to exhibit a low and relatively stable thermal conductivity (0.219–0.267 W m^{-1} K^{-1}) over a temperature range of 298–673 K (Fig. 6(c)), which indicates that the thermal conductivity of CoNi/MXene@Wood-1.5 does not significantly change with the environment. In addition, CoNi/MXene@Wood-1.5 can provide satisfactory thermal camouflage for protected targets in different environments.

To verify this, samples were placed on heating plates at different temperatures to simulate targets with different temperatures, and their thermographic images were recorded using infrared camera. We used ice placed at room temperature to simulate a situation where the target temperature is lower than the background temperature. In the thermal images, a clear radiometric contrast appears between the target and the background, but the area covered with CoNi/MXene@Wood-1.5 is essentially the same as the background (Fig. 6(e)). Moreover, a more general case of thermal stealth was simulated at different temperatures, where a hot target was hidden in a relatively cooler background. As shown in Fig. 6(e), when the temperature of the hot plate increased from 330.50 K to 362.67 K, the temperature of the CoNi/MXene@Wood-1.5-covered area only increased from 306.75 K to 320.28 K due to the satisfactory thermal insurance performance, thus effectively weakening the radiation contrast between the protected target and the background.

Conclusion

Herein, we demonstrated the preparation of the CoNi/MXene@Wood absorber, which involved the carbonization of natural wood at high temperatures and the introduction of CoNi and $Ti_3C_2T_x$ MXene into its rectangular honeycomb unit through hydrothermal reaction and vacuum impregnation. This material can be used for electromagnetic protection and infrared stealth. The RL_{min} value of CoNi/MXene@Wood-1.5 is as high as −56.8 dB, and the EAB can cover the entire X-band. This excellent performance was attained from the rational control of the structure and composition, which enables the composite to optimize the polarization loss, increase the magnetic coupling loss, and establish a multi-dimensional dielectric loss network space. In addition, the synergistic effect of structure and composition, with stable low thermal conductivity (0.219–0.267 W m^{-1} K^{-1}) over a temperature range of 298–673 K, can achieve thermal infrared stealth of protected targets in different environments. The multifunctional CoNi/MXene@Wood absorber opens the door for the design of highly efficient EMA materials in complex environments.

Author contributions

Yuanyuan Li: writing – original draft, writing – review and editing, formal analysis, data curation, investigation, validation. Zhe Zou: writing – review and editing, data curation. Mingqiang Ning: conceptualization, writing – review and editing, data curation, and funding acquisition. Ming Gao and Qikui Man: resources and project administration.

Conflicts of interest

There are no conflicts to declare.

Data availability

All data supporting the findings of this study are available within the main text. All relevant data are available from the corresponding authors upon reasonable request.

Acknowledgements

The authors gratefully acknowledge the financial support by the National Natural Science Foundation of China (grant no. 52102370), the Jiangxi Provincial Major Science and Technology Project (grant no. 20233AAE02007), the Key Research and Development Program of Zhejiang Province (grant no. 2024C01157), the Natural Foundation of Ningbo (grant no. 2023J361), and the Ningbo Key Research and Development Program (grant no. 2022Z192).

References

1 Q. Du, Q. Men, R. Li, Y. Cheng, B. Zhao and R. Che, *Small*, 2022, **18**, 2203609.
2 X. Zhang, B. Li, J. Xu, X. Zhang, Y. Shi, C. Zhu, X. Zhang and Y. Chen, *Adv. Funct. Mater.*, 2023, **33**, 2210456.
3 J. Luo, M. Feng, Z. Dai, C. Jiang, W. Yao and N. Zhai, *Nano Res.*, 2022, **15**, 5781–5789.
4 M. Zhou, W. Gu, G. Wang, J. Zheng, C. Pei, F. Fan and G. Ji, *J. Mater. Chem. A*, 2020, **8**, 24267–24283.
5 Z. Wu, H. W. Cheng, C. Jin, B. Yang, C. Xu, K. Pei, H. Zhang, Z. Yang and R. Che, *Adv. Mater.*, 2022, **34**, 2107538.
6 M. Ning, P. Jiang, W. Ding, X. Zhu, G. Tan, Q. Man, J. Li and R. W. Li, *Adv. Funct. Mater.*, 2021, **31**, 2011229.
7 J. Song, Y. Gao, G. Tan, Q. Man and Z. Wang, *Ceram. Int.*, 2022, **48**, 22896–22905.
8 Q. Ban, Y. Li, Y. Qin, Y. Zheng, X. Xie, Z. Yu and J. Kong, *J. Colloid Interface Sci.*, 2022, **616**, 618–630.
9 H. Zhang, C. Shi, Z. Jia, X. Liu, B. Xu, D. Zhang and G. Wu, *J. Colloid Interface Sci.*, 2021, **584**, 382–394.
10 F. Meng, H. Wang, F. Huang, Y. Guo, Z. Wang, D. Hui and Z. Zhou, *Composites, Part B*, 2018, **137**, 260–277.
11 R. Kumar, S. Sahoo, E. Joanni, R. K. Singh, W. K. Tan, K. K. Kar and A. Matsuda, *Carbon*, 2021, **177**, 304–331.
12 X. Zhang, J. Qiao, Y. Jiang, F. Wang, X. Tian, Z. Wang, L. Wu, W. Liu and J. Liu, *Nano-Micro Lett.*, 2021, **13**, 135.
13 H. Cheng, Y. Pan, X. Wang, C. Liu, C. Shen, D. W. Schubert, Z. Guo and X. Liu, *Nano-Micro Lett.*, 2022, **14**, 116.
14 M. Ning, Z. Lei, G. Tan, Q. Man, J. Li and R.-W. Li, *ACS Appl. Mater. Interfaces*, 2021, **13**, 47061–47071.
15 Z. Guo, P. Ren, F. Yang, T. Wu, L. Zhang, Z. Chen and F. Ren, *Composites, Part B*, 2023, **263**, 110863.
16 S. Li, W. Mo, Y. Liu and Q. Wang, *Chem. Eng. J.*, 2023, **454**, 140133.
17 Y. Xiong, L. Xu, C. Yang, Q. Sun and X. Xu, *J. Mater. Chem. A*, 2020, **8**, 18863–18871.
18 Z. Gao, Y. Shi, L. Ma, J. Du and J. Qiu, *ACS Appl. Mater. Interfaces*, 2024, **16**, 49687–49700.
19 J. Yan, C. Lin, S. Jiang, W. Wang, M. Zhong, H. Tang and R. Guo, *Chem. Eng. J.*, 2024, **499**, 156409.
20 Q. Wang, J. Zhang, Z. Zhou, J. Zhao, Y. Yi, S. Feng, Z. Sui, W. Zhang and C. Lu, *Small*, 2024, **20**, 2309803.
21 Z. Chu, D. Chen, Q. Huang, Y. Li, Z. Wu, Y. Yang and Z. Yang, *Ind. Crops Prod.*, 2022, **187**, 115387.
22 C. Chen, Y. Zhang, Y. Li, J. Dai, J. Song, Y. Yao, Y. Gong, I. Kierzewski, J. Xie and L. Hu, *Energy Environ. Sci.*, 2017, **10**, 538–545.
23 L. L. Lu, Y. Y. Lu, Z. J. Xiao, T. W. Zhang, F. Zhou, T. Ma, Y. Ni, H. B. Yao, S. H. Yu and Y. Cui, *Adv. Mater.*, 2018, **30**, 1706745.
24 J. Xi, E. Zhou, Y. Liu, W. Gao, J. Ying, Z. Chen and C. Gao, *Carbon*, 2017, **124**, 492–498.
25 M. Qiao, J. Li, S. Li, D. Wei, X. Lei, W. Lei, J. Wei, Q. Zhang and M. Ma, *J. Alloys Compd.*, 2022, **926**, 166854.
26 Y. Zhao, W. Wang, J. Wang, J. Zhai, X. Lei, W. Zhao, J. Li, H. Yang, J. Tian and J. Yan, *Carbon*, 2021, **173**, 1059–1072.
27 X. Guo, Z. Nie, Y. Feng, M. Jiang, Z. Zhao, X. Yang, R. Wang and S. Qi, *ACS Appl. Nano Mater.*, 2024, **7**, 19427–19438.
28 Y. Qiu, H. Yang, F. Hu and Y. Lin, *Nano Res.*, 2022, **15**, 7769–7777.
29 Z. Zhang, Z. Cai, Y. Zhang, Y. Peng, Z. Wang, L. Xia, S. Ma, Z. Yin, R. Wang, Y. Cao, Z. Li and Y. Huang, *Carbon*, 2021, **174**, 484–499.
30 Z. Wang, Z. Cheng, C. Fang, X. Hou and L. Xie, *Composites, Part A*, 2020, **136**, 105956.
31 T. Hou, Z. Jia, Y. Dong, X. Liu and G. Wu, *Chem. Eng. J.*, 2022, **431**, 133919.
32 G. Cui, X. Zheng, X. Lv, Q. Jia, W. Xie and G. Gu, *Ceram. Int.*, 2019, **45**, 23600–23610.
33 B. Fan, N. Li, B. Dai, S. Shang, L. Guan, B. Zhao, X. Wang, Z. Bai and R. Zhang, *Adv. Powder Technol.*, 2020, **31**, 808–815.
34 X. Chen, Y. Li, S. Cheng, K. Wu, Q. Wang, L. Liu, F. Yang, A. Xie, H. Pang and C. Yu, *Adv. Funct. Mater.*, 2023, **34**, 2308274.
35 J.-L. Gao, L. Chang, B. Niu, X.-C. Zhang, L. Li and M.-S. Cao, *Adv. Compos. Hybrid Mater.*, 2024, **7**, 103.
36 Z. Zou, M. Ning, Z. Lei, X. Zhuang, G. Tan, J. Hou, H. Xu, Q. Man, J. Li and R.-W. Li, *Carbon*, 2022, **193**, 182–194.
37 S. Zhang, F. Zhang, Y. Xie, H. Niu, Y. Li, H. Wang, R. Zhang, H. Li, X. Wang and B. Fan, *Ceram. Int.*, 2022, **48**, 33751–33762.
38 F. Yang, J. Yao, L. Jin, W. Huyan, J. Zhou, Z. Yao, P. Liu and X. Tao, *Composites, Part B*, 2022, **243**, 110161.
39 F. Pan, Y. Rao, D. Batalu, L. Cai, Y. Dong, X. Zhu, Y. Shi, Z. Shi, Y. Liu and W. Lu, *Nano-Micro Lett.*, 2022, **14**, 140.
40 M.-Q. Ning, M.-M. Lu, J.-B. Li, Z. Chen, Y.-K. Dou, C.-Z. Wang, F. Rehman, M.-S. Cao and H.-B. Jin, *Nanoscale*, 2015, **7**, 15734–15740.
41 M. Ma, Q. Zheng, X. Zhang, L. Li and M. Cao, *Carbon*, 2023, **212**, 118159.
42 J. Yan, Q. Zheng, S. P. Wang, Y. Z. Tian, W. Q. Gong, F. Gao, J. J. Qiu, L. Li, S. H. Yang and M. S. Cao, *Adv. Mater.*, 2023, **35**, 2300015.
43 L. Chang, Y.-Z. Wang, X.-C. Zhang, L. Li, H.-Z. Zhai and M.-S. Cao, *J. Mater. Sci. Technol.*, 2024, **174**, 176–187.
44 X. Jiang, Q. Wang, L. Song, H. Lu, H. Xu, G. Shao, H. Wang, R. Zhang, C. Wang and B. Fan, *Carbon Energy*, 2024, **6**, 502.
45 X. Li, S. Yin, L. Cai, Z. Wang, C. Zeng, H. Jiang, J. Cheng and W. Lu, *Chem. Eng. J.*, 2023, **454**, 140127.

46 Y. Wang, N. Li, G. W. Huang, Y. Liu, S. Z. Li, R. X. Cao and H. M. Xiao, *Small Methods*, 2025, 2401982.
47 G. Ding, C. Sun, M. Wang, Y. Hu, G. Cheng and J. Liu, *Mater. Res. Bull.*, 2025, **181**, 113121.
48 B. Kang, C. Bai, L. Huang, C. Zhu, X. Zhang and Y. Chen, *Mater. Res. Bull.*, 2025, **187**, 113395.
49 J. Wang, L. Zhang, J. Yan, J. Yun, W. Zhao, K. Dai, H. Wang and Y. Sun, *Adv. Funct. Mater.*, 2024, **34**, 2402419.
50 X.-Y. Fu, Q. Zheng, L. Li and M.-S. Cao, *Carbon*, 2022, **197**, 324–333.
51 Y. Bao, S. Guo, Y. Li, Z. Jia, H. Guan, D. Lei, J. Chen, B. Zhong and Z. Li, *ACS Appl. Electron. Mater.*, 2023, **5**, 227–239.
52 J.-x. Dai and G.-l. Xu, *J. Magn. Magn. Mater.*, 2023, **568**, 170405.
53 Y. He, Q. Su, D. Liu, L. Xia, X. Huang, D. Lan, Y. Liu, Y. Huang and B. Zhong, *Chem. Eng. J.*, 2024, **491**, 152041.
54 H. Wang, J. Zhao, Z. Wang and P. Liu, *ACS Appl. Mater. Interfaces*, 2023, **15**, 4580–4590.
55 J. Xu, Z. Wang, C. Ge, X. Qi, Q. Bao and C. Liu, *J. Colloid Interface Sci.*, 2025, **677**, 529–539.
56 L. Yu, Q. Zhu, Z. Guo, Y. Cheng, Z. Jia and G. Wu, *J. Mater. Sci. Technol.*, 2024, **170**, 129–139.
57 L. Yu, D. Lan, Z. Guo, A. Feng, G. Wu, Z. Jia, X. Feng and P. Yin, *J. Mater. Sci. Technol.*, 2024, **189**, 155–165.